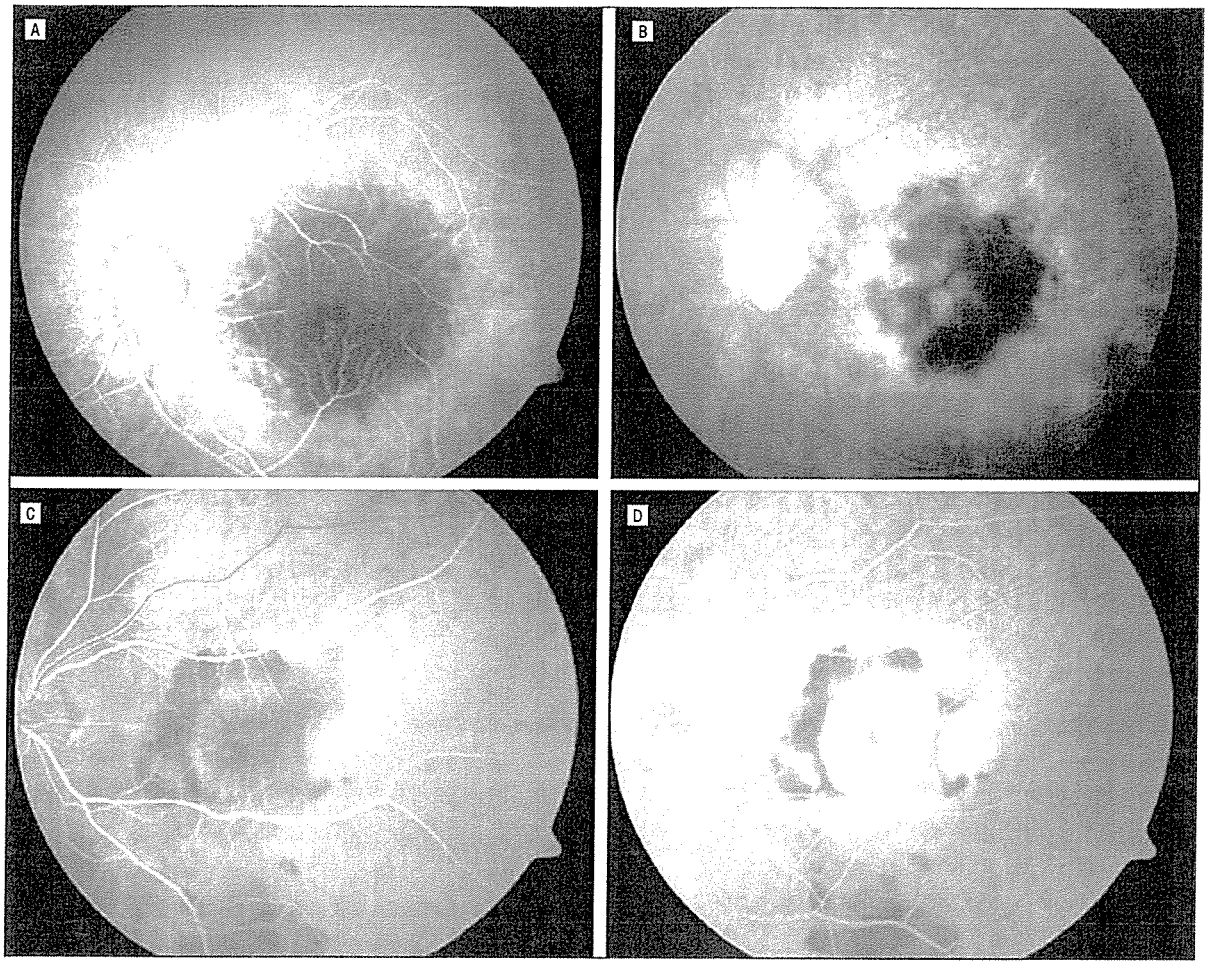

Figure 1. Fluorescein angiographs taken on the day of surgical extraction of the choroidal neovascular membrane. A, Early phase of fluorescein angiography 3 days after photodynamic therapy in case 4. B, Late phase of fluorescein angiography 3 days after photodynamic therapy in case 4. C, Early phase of fluorescein angiography 34 days after photodynamic therapy in case 5. D, Late phase of fluorescein angiography 34 days after photodynamic therapy in case 5.

in 2 cases and relatively abundant (n = 36) only in 1 specimen with the lowest percentage of occluded vessels (Figure 2A). The proliferative activity in specimens extracted 3 days after PDT (median proliferative activity, 4.85 nuclei/mm^2; range, 0-9.71 nuclei/mm^2) was smaller than that in the CNV membranes without prior PDT (median proliferative activity 53.20 nuclei/mm^2; range, 0-514.08 nuclei/mm^2), but this difference did not reach statistical significance (P = .13). However, at longer intervals following PDT, proliferative activity increased significantly (median proliferative activity, 78.28 nuclei/mm^2; range, 0-829.29 nuclei/mm^2) (P = .04) (Figure 2A and Figure 3F).

EXPRESSION OF VEGF

In CNV membranes not treated with PDT, VEGF staining was absent in the RPE cells of 18 (60.0%) of 30 specimens (Figure 2B). In the remaining 12 (40.0%) of 30 specimens, VEGF staining was mostly weak to moderate (**Figure 4**A and B). A moderate amount of VEGF expression was found in 16 (53.3%) of 30 vascular endothelial cells. Only 4 (13.3%) of 30 specimens, however, displayed intense staining (Figure 2B). The VEGF staining within the stroma appeared in both fibroblast-like and inflammatory cells (Figure 2B and Figure 4A and B).

In all of the membranes extracted 3 days after PDT (n = 4), cytokeratin 18–positive RPE cells (Figure 4C) showed an intense staining for VEGF (Figure 2B and Figure 4C and D). At longer posttreatment intervals, the VEGF staining in RPE cells persisted to different degrees (Figure 2B and Figure 4F), being absent in only 2 cases. Three days after PDT, only 1 membrane had endothelial cells with a moderate expression of VEGF. The other 3 specimens were either negative for staining (n = 1) or were just weakly stained (n = 2). At greater intervals (n = 16), the VEGF staining in endothelial cells appeared to increase, with only 1 case of endothelial cells without VEGF staining, and 10 (66.7%) of 15 specimens had moderate to intense staining at the vessels (Figure 2B and Figure 4E and F). The VEGF staining was significantly increased in RPE cells (P<.001), endothelial cells (P = .008), and stromal cells (P = .02) after PDT (Figure 2B and Figure 4E and F). The VEGF staining in-

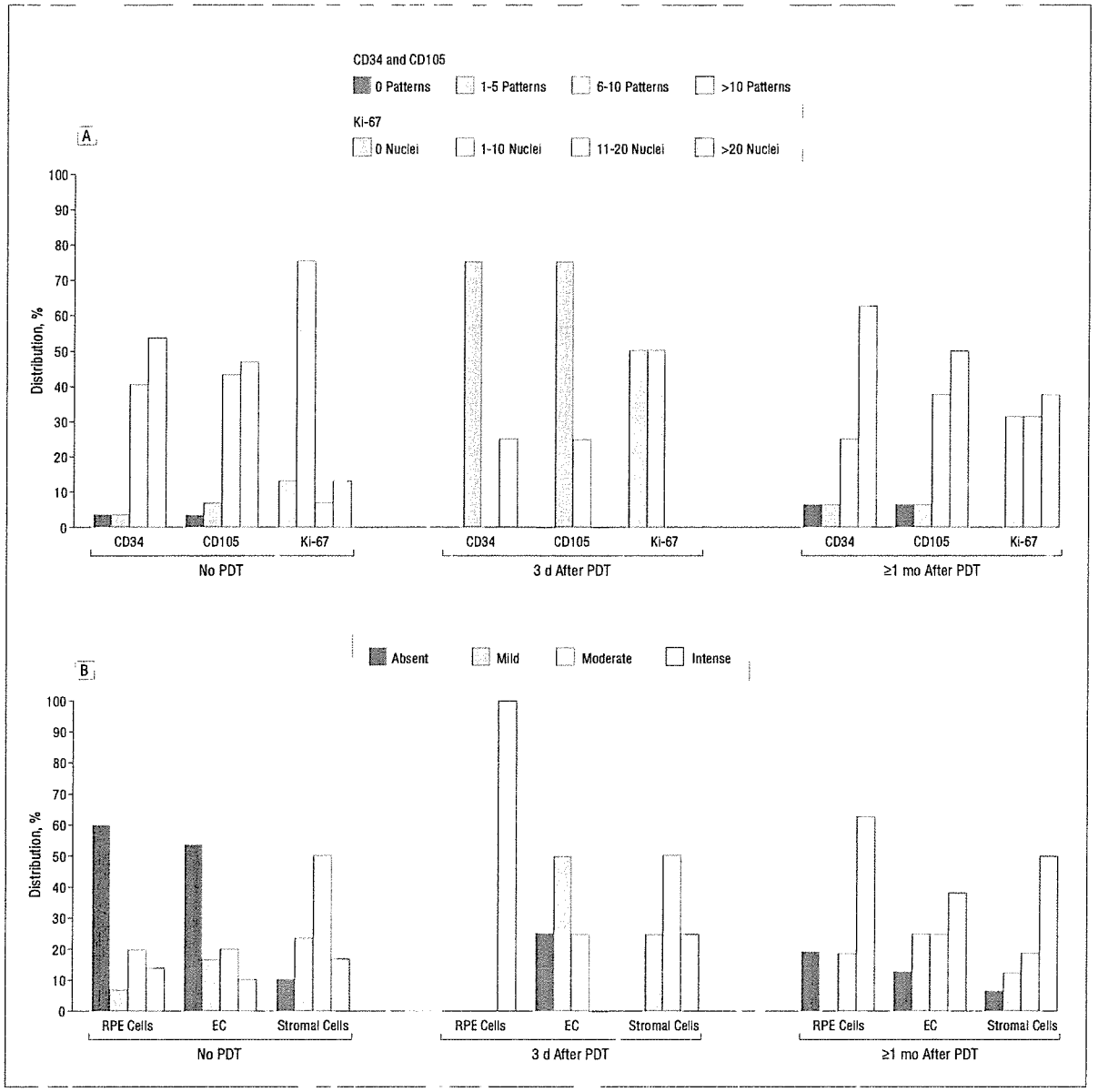

Figure 2. The distribution of endothelial cells (EC) (with vascularization calculated by counting the number of CD34- and CD105-positive vascular-like patterns in the most vascularized area under 200 magnification) and proliferation marker (with proliferative activity evaluated by counting the absolute number of Ki-67–positive nuclei within the specimen) (A) and of vascular endothelial growth factor (with vascular endothelial growth factor immunostaining in retinal pigment epithelial [RPE] cells, EC, and stromal cells evaluated separately and semiquantitatively) (B) in choroidal neovascularization without pretreatment, 3 days after photodynamic therapy (PDT), and 1 or more months after PDT

tensity showed no predilection according to the localization in the CNV

COMMENT

Lately PDT has gained an important role in the treatment of neovascular AMD. The potential and benefit of this therapy however are compromised by high recurrence rates and a reduced functional prognosis. To promote this treatment concept and to reduce its limitations, knowledge of the biological effects of PDT in CNV is crucial.

Choroidal neovascularization is most likely the result of neoangiogenesis, and VEGF is thought to play a pivotal role within this process.[9-15] Vascular endothelial growth factor has been shown to be required for normal vascular development,[16] survival and morphology of choriocapillaris,[17] and retinal neovascularization[18] in experimental animal models. It plays a key role in the pathogenesis of ischemia-associated retinal neovascularization[19] and is a major stimulator of CNV development and growth.[14] Vascular endothelial growth factor is present both in surgically excised CNV membranes from human eyes with AMD[9-12] and in experimental CNV membranes.[1] It can induce CNV

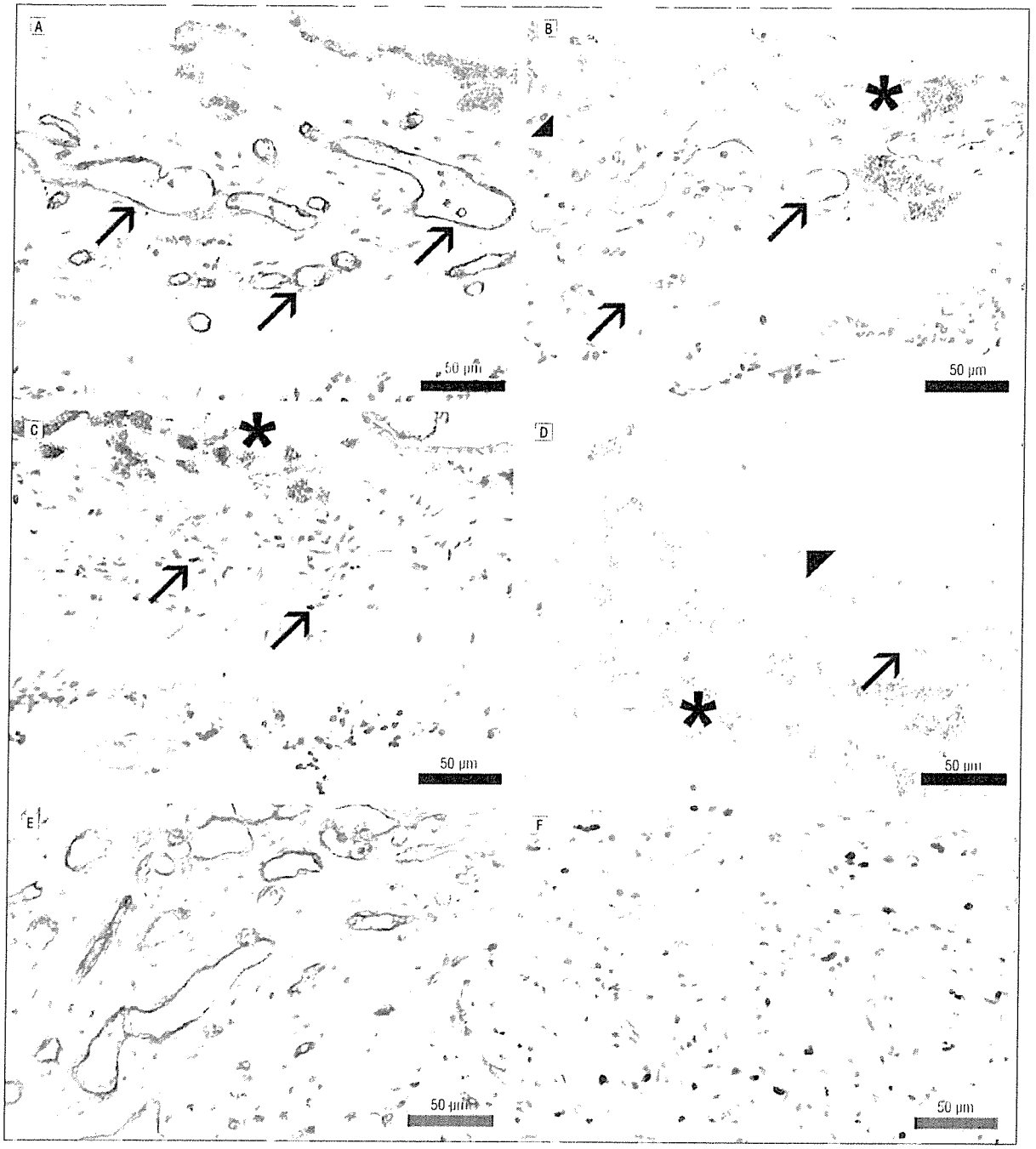

Figure 3. Photomicrographs of a surgically excised choroidal neovascular membrane. The specimen of a case that did not receive photodynamic therapy was probed with antibodies against CD34 (A) and CD105 (B), stained with 3-diaminobenzidine (resulting in a brown chromogen), and counterstained with hematoxylin. The endothelial cell markers CD34 and CD105 are selectively expressed in vascular structures (arrows). Some endothelial cells do not stain for CD105 (arrowhead). The brown chromogen can be distinguished from the melanin granula (asterisk) contained in pigmented cells. C, In the same case that did not receive photodynamic therapy, several cell nuclei express the proliferation marker Ki-67 (arrows). The brown chromogen can be distinguished from the melanin granula (asterisk) contained in pigmented cells. D, The choroidal neovascular membrane from case 2 extracted 3 days after photodynamic therapy was probed with CD34. Some of the vessels shown by the brown chromogen are still patent (arrow) whereas others appear collapsed (arrowhead). The brown chromogen can be distinguished from the melanin granula (asterisk) contained in pigmented cells. A choroidal neovascular membrane (case 7) extracted 40 days after photodynamic therapy shows the brown chromogen from the stain by CD105 with patent and vital looking vessels (E) and by Ki-67 with several proliferating cells (brown nuclei) (F).

in animal models,[17] and CNV has been suppressed by anti-VEGF therapy in primates.[1]

To understand the changes that might be related to PDT we first examined CNV membranes that did not receive PDT before surgery. In our study VEGF expression by RPE cells could be detected in fewer than 50% of the cases, with intense expression in only 13% of the membranes. In contrast, expression by stromal cells was

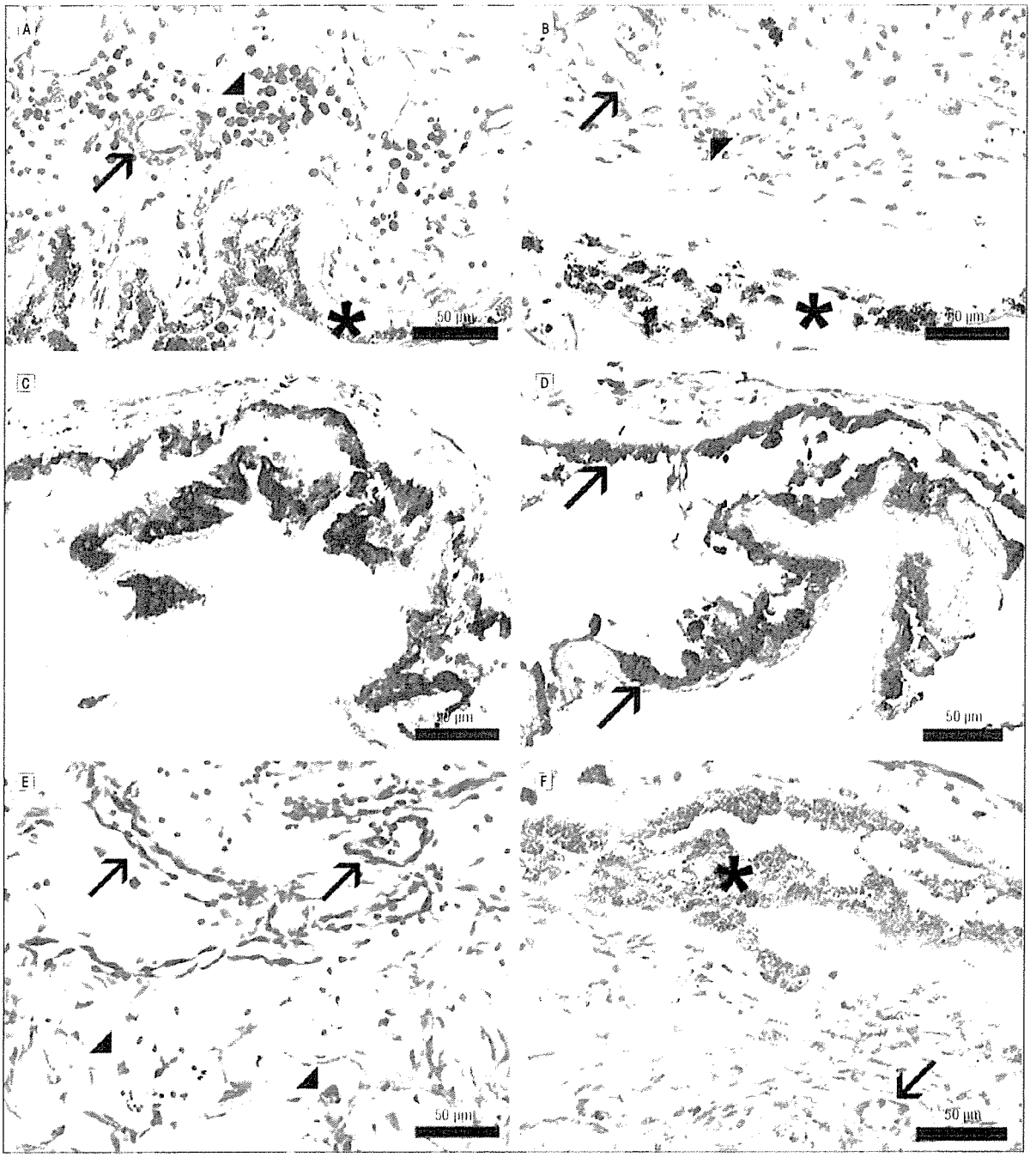

Figure 4. Photomicrographs of surgically excised choroidal neovascular membranes. A, A specimen that did not receive photodynamic therapy was stained for vascular endothelial growth factor (VEGF) (red chromogen) and showed a retinal pigment epithelial (RPE) cell layer (asterisk), vascularization (arrow), fibroblastic stromal cells, and different degrees of an inflammatory infiltration (arrowhead). The VEGF staining can be detected within inflammatory, endothelial, and stromal cells. B, Another specimen that did not receive photodynamic therapy was stained for VEGF (red chromogen) and showed an RPE cell layer (asterisk), vascularization (arrow), fibroblastic stromal cells, and different degrees of an inflammatory infiltration (arrowhead). The VEGF staining can be detected within endothelial and stromal cells whereas RPE cells are negative for staining. A choroidal neovascular membrane from case 2 was extracted 3 days after photodynamic therapy and stained (red chromogen) for cytokeratin 18 (C) and VEGF (where the RPE cells [arrows] were strongly positive for VEGF as compared with the choroidal neovascular membranes that were not treated with photodynamic therapy) (D). Specimens from cases 7 (E) and 11 (F) were stained for VEGF (red chromogen), and VEGF was expressed by endothelial cells (arrows), stromal cells (arrowheads), and RPE cells (E) (asterisk).

found in 90% of the cases. These results confirm the findings by Kvanta et al,[10] who detected VEGF staining and VEGF messenger RNA expression particularly in fibroblast-like cells but only occasionally in RPE cells of human CNV membranes. Lopez et al[11] described VEGF production by RPE cells, endothelial cells, fibroblasts, macrophages, and monocytes in CNV membranes. In our membranes, VEGF staining in endothelial, RPE, and stro-

mal cells at different intensities was in concordance with their findings.

In our series of 20 patients receiving presurgical PDT 4 membranes were extracted 3 days after PDT. Fluorescein angiography on the day of surgery revealed nonperfusion of the CNV within the area of the laser treatment as demonstrated by the occlusion of most of the vessels both within the CNV and in the surrounding normal choroid.[20,21] Histological analysis of PDT-treated human eyes supported these findings by identifying an occluded choriocapillary layer within the spot produced by the laser.[22,23] We detected as an early change many collapsed vessels as well as several patent vessels with presumably damaged endothelial cells. The proliferative activity within these specimens was low.[20] Interestingly, in all of these membranes, intense VEGF staining was extremely prominent in RPE cells whereas it varied in endothelial and stromal cells. Vascular endothelial growth factor is known to be strongly induced by hypoxia in RPE cells[24] as well as by reactive oxygen intermediates.[25] Either aggravated hypoperfusion of the choroid[21,26-28] and/or reactive oxygen intermediates released by the photochemical effect of PDT might be the angiogenic stimuli inducing VEGF secretion by RPE cells after PDT.

Whatever reason might be responsible, enhanced VEGF expression by RPE cells, even when temporary, is an important angiogenic stimulus that leads to increased vascular leakage and development of CNV.[29] In fact, CNV membranes extracted at longer intervals after PDT showed patent vessels lined by healthy endothelial cells that were highly positive for CD34 and CD105. None of these 16 specimens had occluded or collapsed vessels. The proliferative activity was significantly increased and associated with a cell-rich fibrocellular stroma and an inflammatory response. The VEGF expression by RPE cells persisted in most of these cases. In contrast, the VEGF expression in endothelial and stromal cells appeared to be enhanced compared with the early post-PDT cases. The high inflammatory activity appearing in the longer post-PDT intervals may also be a factor in sustaining increased VEGF expression.

Bula et al[30] examined VEGF expression in 6 CNV membranes extracted 3 months after PDT. Four CNV membranes without prior PDT composed the control group. Contrary to our results, no significant difference in VEGF expression was detected between the treated and untreated CNV membranes. The small number of specimens as well as the long post-PDT interval in their work might be responsible for their results.

The number of retreatments did not seem to affect the chronology of the process that is induced by the last treatment. Although it is a mild and selective modality, PDT is still a traumatizing event inducing a wound-healing cascade with the initial characteristics of angiogenesis within an inflammatory setting. In fact, although all of the membranes appear to be inflammatory inactive and nonproliferative 3 days after PDT, there seems to be a rebound activity thereafter.

When applied to normal chorioretinal structures, PDT increased VEGF expression in endothelial cells of the choriocapillaris, but not at the level of that in the RPE cells.[31] However, in our study, PDT applied to CNV induced an early VEGF response by RPE cells.

Our results may explain the clinical observation of a decreased retreatment rate and an increased visual improvement when PDT is combined with anti-VEGF treatment.[32,33] Intravitreal injections of anti-VEGF molecules should interrupt the vicious cycle induced by PDT. In a phase II study,[33] anti-VEGF aptamer was injected intravitreally 5 to 10 days after PDT. Prominent VEGF expression in RPE cells already 3 days after PDT in our samples, however, suggests an earlier anti-VEGF intervention.

To our knowledge, this is the first clinicopathological correlation of changes regarding VEGF expression, proliferative activity, and vascularization in CNV membranes treated with PDT. The proper interpretation of this study, however, is limited by the fact that our cases may represent a negative selection. Although the histopathological findings in patients who benefit from verteporfin PDT might differ, it is conceivable that PDT causes trauma followed by enhanced VEGF expression and angiogenesis associated with an inflammatory wound-healing process. With regard to the reinitiation of the angiogenic cascade, the need for a counteracting adjunctive therapy started at the proper time becomes more and more obvious.[4]

Submitted for Publication: February 23, 2005; final revision received July 12, 2005; accepted July 21, 2005.
Correspondence: Salvatore Grisanti, MD, Department of Ophthalmology, Division of Vitreoretinal Surgery, Eberhard-Karls-University Tübingen, Schleichstrasse 12-15, 72076 Tübingen, Germany (salvatore.grisanti@med.uni-tuebingen.de).
Financial Disclosure: None.
Funding/Support: This work was supported by the Grimmke Foundation, the Jung Foundation, and the Vision 100 Foundation.

REFERENCES

1. Ghafour IM, Allan D, Foulds WS. Common causes of blindness and visual handicap in the west of Scotland. *Br J Ophthalmol*. 1983;67:209-213.
2. Hyman L. Epidemiology of eye disease in the elderly. *Eye*. 1987;1:330-341.
3. Schmidt-Erfurth U, Hasan T. Mechanisms of action of photodynamic therapy with verteporfin for the treatment of age-related macular degeneration. *Surv Ophthalmol*. 2000;45:195-214.
4. Treatment of Age-Related Macular Degeneration With Photodynamic Therapy (TAP) Study Group. Photodynamic therapy of subfoveal choroidal neovascularization in age-related macular degeneration with verteporfin: one-year results of 2 randomized clinical trials: TAP report 1. *Arch Ophthalmol*. 1999;117:1329-1345.
5. Treatment of Age-Related Macular Degeneration With Photodynamic Therapy (TAP) Study Group. Photodynamic therapy of subfoveal choroidal neovascularization in age-related macular degeneration with verteporfin: two-year results of 2 randomized clinical trials: TAP report 2. *Arch Ophthalmol*. 2001;119:198-207.
6. Treatment of Age-Related Macular Degeneration With Photodynamic Therapy (TAP) Study Group. Verteporfin therapy of subfoveal choroidal neovascularization in patients with age-related macular degeneration: additional information regarding baseline lesion composition's impact on vision outcomes: TAP report No. 3. *Arch Ophthalmol*. 2002;120:1443-1454.
7. Verteporfin in Photodynamic Therapy Study Group. Verteporfin therapy of subfoveal choroidal neovascularization in age-related macular degeneration: two-year results of a randomized clinical trial including lesions with occult with no classic choroidal neovascularization: Verteporfin in photodynamic therapy report 2. *Am J Ophthalmol*. 2001;131:541-560.
8. Blinder KJ, Bradley S, Bressler NM, et al; Treatment of Age-related Macular Degeneration With Photodynamic Therapy Study Group; Verteporfin in Photodynamic Therapy Study Group. Effect of lesion size, visual acuity, and lesion composition on visual acuity change with and without verteporfin therapy for choroidal neovascularization secondary to age-related macular degeneration: TAP and VIP report No. 1. *Am J Ophthalmol*. 2003;136:407-418.

9. Grossniklaus HE, Ling JX, Wallace TM, et al. Macrophage and retinal pigment epithelium expression of angiogenic cytokines in choroidal neovascularization. *Mol Vis.* 2002;8:119-126.
10. Kvanta A, Algvere PV, Berglin L, Seregard S. Subfoveal fibrovascular membranes in age-related macular degeneration express vascular endothelial growth factor. *Invest Ophthalmol Vis Sci.* 1996;37:1929-1934.
11. Amin R, Puklin JE, Frank RN. Growth factor localization in choroidal neovascular membranes of age-related macular degeneration. *Invest Ophthalmol Vis Sci.* 1994;35:3178-3188.
12. Lopez PF, Sippy BD, Lambert HM, Thach AB, Hinton DR. Transdifferentiated retinal pigment epithelial cells are immunoreactive for vascular endothelial growth factor in surgically excised age-related macular degeneration-related choroidal neovascular membranes. *Invest Ophthalmol Vis Sci.* 1996;37:855-868.
13. Wada M, Ogata N, Otsuji T, Uyama M. Expression of vascular endothelial growth factor and its receptor (KDR/flek-1) mRNA in experimental choroidal neovascularization. *Curr Eye Res.* 1999;18:203-213.
14. Kwak N, Okamoto N, Wood J, Campochiaro P. VEGF is major stimulator in model of choroidal neovascularization. *Invest Ophthalmol Vis Sci.* 2000;41:3158-3164.
15. Krzystolik MG, Afshari MA, Adamis AP, et al. Prevention of experimental choroidal neovascularization with intravitreal anti-vascular endothelial growth factor antibody fragment. *Arch Ophthalmol.* 2002;120:338-346.
16. Carmeliet P, Ferreira V, Breier G, et al. Abnormal blood vessel development and lethality in embryos lacking a single VEGF allele. *Nature.* 1996;380:435-439.
17. Blaauwgeers HG, Holtkamp GM, Rutten H, et al. Polarized vascular endothelial growth factor secretion by human retinal pigment epithelium and localization of vascular endothelial growth factor receptors on the inner choriocapillaris: evidence for a trophic paracrine relation. *Am J Pathol.* 1999;155:421-428.
18. Aiello LP, Pierce EA, Foley ED, et al. Suppression of retinal neovascularization in vivo by inhibition of vascular endothelial growth factor (VEGF) using soluble VEGF-receptor chimeric proteins. *Proc Natl Acad Sci U S A.* 1995;92:10457-10461.
19. Smith LE, Wesolowski E, McLellan A, et al. Oxygen-induced retinopathy in the mouse. *Invest Ophthalmol Vis Sci.* 1994;35:101-111.
20. Grisanti S, Tatar O, Canbek S, et al. Immunohistopathologic evaluation of choroidal neovascular membranes following verteporfin photodynamic therapy. *Am J Ophthalmol.* 2004;137:914-923.
21. Michels S, Schmidt-Erfurth U. Sequence of early vascular events after photodynamic therapy. *Invest Ophthalmol Vis Sci.* 2003;44:2147-2154.
22. Schmidt-Erfurth U, Laqua H, Schlötzer-Schrehardt U, Viestenz A, Naumann GOH. Histopathological changes following photodynamic therapy in human eyes. *Arch Ophthalmol.* 2002;120:835-844.
23. Schlötzer-Schrehardt U, Viestenz A, Naumann GOH, Laqua H, Michels S, Schmidt-Erfurth U. Dose-dependent structural effects of photodynamic therapy on choroidal and retinal structures of human eyes. *Graefes Arch Clin Exp Ophthalmol.* 2002;240:748-757.
24. Shima DT, Adamis AP, Ferrara N, et al. Hypoxic induction of endothelial cell growth factors in retinal cells: identification and characterization of vascular endothelial growth factor (VEGF) as the mitogen. *Mol Med.* 1995;1:182-193.
25. Kuroki M, Voest EE, Amano S, et al. Reactive oxygen intermediates increase vascular endothelial growth factor expression in vitro and in vivo. *J Clin Invest.* 1996;98:1667-1675.
26. Schmidt-Erfurth UM, Michels S. Changes in confocal indocyanine green angiography through two years following photodynamic therapy with verteporfin *Ophthalmology.* 2003;110:1306-1314.
27. Schmidt-Erfurth U, Michels S, Barbazetto I, Laqua H. Photodynamic effects on choroidal neovascularization and physiological choroids. *Invest Ophthalmol Vis Sci.* 2002;43:830-841.
28. Schlingemann RO. Role of growth factors and the wound healing response in age-related macular degeneration. *Graefes Arch Clin Exp Ophthalmol.* 2004;242:91-101.
29. Spilsbury K, Garrett KL, Shen WY, Constable IJ, Rakoczy PE. Overexpression of vascular endothelial growth factor (VEGF) in the retinal pigment epithelium leads to the development of choroidal neovascularization. *Am J Pathol.* 2000;157:135-144.
30. Bula DV, Iliaki E, Gragoudas E, Miller JW, Arroyo J. Pigment epithelium–derived factor, angiopoietin-1, and VEGF expression in human choroidal neovascular membranes treated with photodynamic therapy [ARVO abstract]. *Invest Ophthalmol Vis Sci.* 2004;45:E-abstract 1787. http://www.iovs.org. Accessed February 15, 2005.
31. Schmidt-Erfurth U, Schlötzer-Schrehard U, Cursiefen C, Michels S, Beckendorf A, Naumann GOH. Influence of photodynamic therapy on expression of vascular endothelial growth factor (VEGF), VEGF receptor 3, and pigment epithelium–derived factor. *Invest Ophthalmol Vis Sci.* 2003;44:4473-4480.
32. Eyetech Study Group. Preclinical and phase 1A clinical evaluation of an anti-VEGF pegylated aptamer (EYE001) for the treatment of exudative age-related macular degeneration. *Retina.* 2002;22:143-152.
33. Eyetech Study Group. Anti-vascular endothelial growth factor therapy for subfoveal choroidal neovascularization secondary to age-related macular degeneration: phase II study results. *Ophthalmology.* 2003;110:979-986.
34. Gragoudas ES, Adamis AP, Cunningham ET Jr, Feinsod M, Guyer DR; VEGF Inhibition Study in Ocular Neovascularization Clinical Trial Group. Pegaptanib for neovascular age-related macular degeneration. *N Engl J Med.* 2004;351:2805-2816.

複視に対するプリズム適応の検討

稲垣理佐子・浅野　麻衣・正木勢津子・彦谷　明子・堀田　喜裕
佐藤　美保

浜松医科大学眼科

Indications of prism prescription for diplopia

Risako Inagaki, Mai Asano, Setsuko Masaki, Akiko Hikoya,
Yoshihiro Hotta, Miho Sato

Department of Ophthalmology, Hamamatsu University School of Medicine

要　約

【複視に対するプリズム適応の検討】

〈目　　的〉処方されたプリズムに満足した症例としなかった症例を比較することによって、不満足であった原因を検討する。

〈対象と方法〉平成15年1月～平成17年5月に複視を主訴に浜松医科大学眼科を受診した20歳以上の患者、総数144名のうち眼位の記載が不十分のもの、追跡ができなかったものを除く86名を対象とした。

プリズム眼鏡を処方され満足した適応群と処方を受けなかったか、受けても不満足であった不適応群に分け性別、年齢、診断、視力、眼位、について検討した。

〈結　　果〉86名のうち、自然治癒は12名、適応群は33名、不適応群はプリズム処方で不満足17名および手術24名をあわせた41名であった。水平、回旋斜視角で適応群、不適応群の二群間に有意差はなかったが、上下斜視角では有意差を認めた。また、上斜筋麻痺では、年齢および上下斜視角で有意差を認めたが、上斜筋麻痺以外で有意差は認められなかった。

〈結　　論〉プリズムを勧めて満足できたものは対象者の半数以下であった。また、プリズムに適応できるかどうかは上下斜視角の程度に強く影響された。疾患別では、若年齢の上斜筋麻痺患者は斜視角が大きく、プリズムに満足しないことが多かったが、上斜筋麻痺以外では二群間に統計的に明らかな要因は認められず、症例ごとにトライアルをする必要があると思われた。

別冊請求先（〒431-3192）浜松市半田山1－20－1
Tel. 053－435－2656　Fax. 053－435－2656

Key words：prism prescription, diplopia, superior oblique palsy
プリズム処方、複視、上斜筋麻痺

Abstract

Purpose

To clarify the reasons of dissatisfaction for prisms by means of comparing the cases who were successfully treated with prisms and the cases who were not.

Subjects and Methods

This is a retrospective chart review.

The patients older than 20 years, who visited Hamamatsu university school of medicine, department of Ophthalmology with a chief complaint of diplopia between January 2003 and May 2005 were studied. Within 144 patients, the patients with insufficient records of eye positions and the patients who were not followed were excluded. The remaining 86 cases were studied.

The patients were divided into two groups: 1) adaptation: who were satisfied with prisms, and 2) non-adaptation: who were not satisfied with prisms. Gender, age, diagnosis, vision, and ocular deviations were compared between the two groups.

Results

Twelve patients did not require prisms because of little trouble and they were excluded from the study. Thirty-three patients were adapted to the prisms. Seventeen patients did not satisfy prisms regardless they were prescribed prisms, and 24 patients underwent strabismus surgery. A total of 41 patients were classified to the non-adapted group.

There were no significant differences between the two groups in age, gender, the amount of horizontal deviation and the amount of torsional deviation. Only the vertical deviation was significantly larger in non-adapted group than in the adapted group (near: $p<0.001$, far: $p<0.0001$). Among the patients with superior oblique palsy, the amount of vertical deviation was larger and the patients were younger in the non-adapted group. These findings were not observed in the patients without superior oblique palsy,

Conclusions

Less than a half of patients satisfied with prisms. The patients' satisfaction was strongly influenced by the amount of vertical deviation. Young patients with superior oblique palsy were unlikely to satisfy with the prisms. It is difficult to speculate the patients who may satisfy with prisms or not. Therefore we need to try prisms on each patient.

Ⅰ．緒　言

複視の治療には手術、視能訓練、光学的治療などがあるが、当院では光学的治療であるプリズム眼鏡を最初に勧めている。しかしプリズム処方には多くの時間と労力がかかり、作成しても使っていないという症例も少なくない。これまでにプリズム処方で満足な結果を得た症例を検討した報告はあるが[1) 2)]、満足と不満足な症例の境界についての情報はあまり見受けられない。そこで、複視を主訴に来院した患者のうちプリズムに満足した症例と、満足しなかった症例を比較検討することによって、プリズムに適応しやすい症例とそうでない症例をあらかじめ予測することが可能になるのではないかと考えた。

本論文の目的は、プリズム装用を勧める患者選択の参考値を求めることである。

Ⅱ．対象および方法

＜対　　象＞

平成15年１月～平成17年５月に複視を主訴に浜松医科大学眼科を受診した20歳以上の患者を、病院の患者情報管理システムを利用して抽出した。144名が抽出されたが、そのうち、眼位の記載が不十分なもの、追跡不可能であったものを除く86名を対象とした。プリズム眼鏡について説明を受けたのち、不自由度が少ないためにプリズム処方を受けずに自然治癒した12名は対

象から除き、74名を以下の方法で二群に分け検討した。対象の振り分けをフローチャートにして図１に示す。プリズムに関する説明を受けた

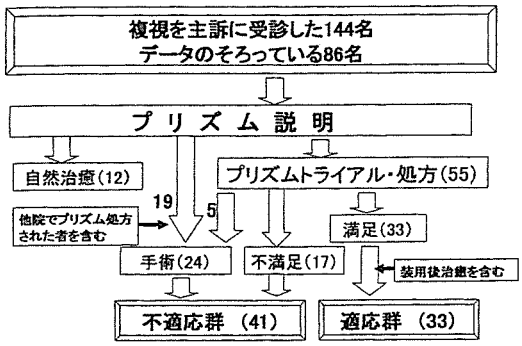

図１　対象の振り分け方法
対象をフローチャートに従って、適応群と不適応群に振り分けた。数字は人数を示す。

段階でプリズム望まなかったのは19名で、残りの55名にトライアルを行った。プリズム処方を受け、再診時にもプリズムを装用していたものは33名であり、適応群とした。その中には装用後に治癒したものも含んでいる。プリズム処方を望まず手術を受けたもの19名、プリズム処方を受けたが不満足でその後手術を受けたもの5名、トライアルの段階で満足が得られなかったか、処方を受けたがプリズムを装用していなかったもの17名の合計41名を不適応群とした。

＜方法１　全体での検討＞

上記の基準で分けた適応群と不適応群の二群間で、性別、年齢、診断、視力、眼位について検討し、有意差検定はMann-Whitney's U testを用い、危険率（ｐ）0.05以下を有意差ありとした。

＜方法２　上斜筋麻痺と甲状腺眼症での検討＞

対象となった症例の中から、症例数の多かった上斜筋麻痺と甲状腺眼症の患者を抽出し、それぞれの中の適応群と不適応群の二群間で、年齢、眼位をMann-Whitney's U testを用いて検討した。

Ⅲ．結　果

＜１．全体での検討＞

疾患別に適応者と不適応者の数を示す。（表１）

適応群と不適応群の間に、性別、年齢、視力に有意差は認められなかった。（表２）

適応群の遠見の水平斜視角は40⊿内斜視～18⊿外斜視、近見の水平斜視角は25⊿内斜視～25⊿外斜視で上下斜視角は遠見、近見とも最高14⊿であった。実際に処方され、満足がえられた水平方向のプリズム度数は平均10.42⊿で範囲は4⊿～21⊿、

表１　対象となった症例の疾患名と人数

疾患名	症例数（適応群）	疾患名	症例数（適応群）
上斜筋麻痺	18（6）	下直筋麻痺	3（2）
甲状腺眼症	9（4）	Brown 症候群	2（1）
外転神経麻痺	5（2）	外斜視	2（2）
糖尿病性眼筋麻痺	4（3）	脳幹梗塞	2（1）
網膜回転術後	4（0）	開散麻痺	1（0）
眼窩底骨折	4（1）	下斜筋過動	1（0）
Skew deviation	3（0）	不明	14（11）

数字は左に全体を、括弧内にプリズムに適応した人数を示す。

表２　適応群と不適応群の性別、年齢、視力

		適応群	不適応群
人数(名)		33	41
性別	男性(名)	23	25
	女性(名)	10	16
年齢（歳）		32～79（平均 59.7）	21～81（平均 52.6）
視力		0.5～2.0（中央値 1.5）	0.1～1.5（中央値 1.2）

表３　適応群の斜視角と処方されたプリズム度数

		範囲	処方プリズム	
			平均	範囲
遠見（⊿）	水平	40ＥＴ～18ＸＴ	10.42	4～21
	上下	0～14	3.3	1～5
近見（⊿）	水平	25ＥＴ～25ＸＴ	10.42	4～21
	上下	0～14	3.3	1～5

ET：内斜視　XT：外斜視

上下方向は平均3.3⊿で範囲は1⊿～5⊿であった。（表３）不適応群の遠見の水平斜視角は45⊿内斜視～50⊿外斜視、近見の水平斜視角は40⊿内斜視～50⊿外斜視で上下斜視角は遠見、近見とも0～35⊿であった。膜プリズムを使用したものが19名、組み込みプリズムが14名、膜プリズムの最高が21⊿、組み込みプリズムの最高は左右合わせて７⊿であった。適応群と不適応群の間に水平斜視角の有意差は見られなかった。しかし上下斜視角の遠見、近見は不適応群の斜視角が大きくなっていた。（p＜0.001）（図２）

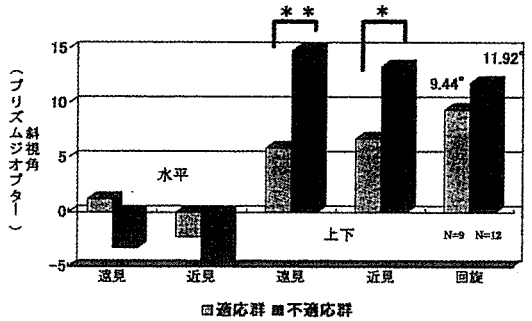

図２　適応群、不適応群の斜視角と回旋偏位度
遠見、近見の水平と上下斜視角の平均を、適応群と不適応群に分けて示す。回旋偏位度の平均を適応群と不適応群に分けて示す。
＊：p＜0.001
＊＊: p<0.0001 (Mann-Whitney's U-test)

回旋複視を合併した21名のうち、プリズムで満足が得られたのは９名で範囲は５°～15°であった。そのうち７名は上下プリズムのみ、１名は一眼に水平プリズム、他眼に上下プリズム、１名は７⊿を基底30°に貼ることで満足な結果がえられた。不適応群は12名で回旋偏位の範囲は３°～30°であった。不適応群12名のうち８名は手術を受けた。適応群と不適応群の間に回旋偏位の有意差は見られなかった。

＜２．上斜筋麻痺と甲状腺眼症での検討＞

上斜筋麻痺では適応群の年齢は66.2±5.24歳、不適応群は39.8±16.5歳で不適応群が若く、上下斜視角では適応群2.75±2.38⊿、不適応群16.42±7.25⊿、で適応群の斜視角が小さいことが判明した。（p＜0.001）（表４）

甲状腺眼症では不適応群が適応群に比べて水平、上下斜視角ともに大きい傾向がみられたが、有意差は認められなかった。（表５）

表４　上斜筋麻痺の検討結果

	適応群（６名）	不適応群（12名）
年齢（歳）	66.2±5.24	39.8±16.5
水平斜視角（⊿）	-3.67±3.50	-8.92±12.01
上下斜視角（⊿）	2.75±2.38	16.42±7.25
回旋偏位（°）	7.67±2.51	7.67±6.43

＊：P<0.01 (Mann-Whitney's U test)

表５　甲状腺眼症の検討結果

	適応群（４名）	不適応群（５名）
年齢（歳）	51.0±4.64	69.8±8.53
水平斜視角（⊿）	-6.38±6.67	3.40±24.02
上下斜視角（⊿）	8.00±2.12	16.60±14.11

いずれも有意差なし

Ⅳ．考　按

今回の調査では水平斜視角よりも上下斜視角が遠見、近見とも不適応群で大きくなっており、適応と不適応群を分ける大きな要因となっていた。その理由について考按する。まず、上下斜視では代償頭位のとりにくさがある。水平斜視でとる代償頭位（顔の回し）よりも上下斜視でとる垂直の代償頭位（顎の上げ下げ）は不自然な姿勢であり不自由度が高いことから、手術を選択することが多いと思われた。次に、高い度数の垂直プリズムを装用すると、プリズムを通して見える眼球の高さが左右でずれるため、美容的に問題になると思われた[3]。（図３）

今回の対象にはさまざまな眼球運動障害が含まれており、各疾患別の症例数は少ないために疾患別の特徴を引き出すには至らなかった。しかし、上斜筋麻痺では適応群６名に対し不適応群12名と不適応群が多く、年齢と斜視角において有意差が現れた。若年性の上斜筋麻痺は先天性、あるいは長期にわたる特発性麻痺のことが多く、加齢により融像が破綻して複視を自覚す

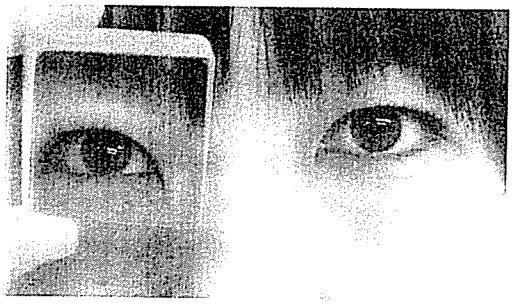

図３　健常者に20⊿を基底90°に装用した場合
プリズムを右眼前に基底上方に装用すると右眼が左眼に比べて下方向にずれているように見えるため、外見的に問題となる。

る。年齢も平均30歳代と若く、自然治癒が望めないとわかった時点で、手術による根治術を望んだと考えられる。それに対し、中高年者の上斜筋麻痺は脳血管障害や外傷による滑車神経麻痺であり、前者とは異なる機序と考えてよい。

今回、満足して装用できたプリズム度数の平均は水平方向10.42⊿、上下方向3.3⊿と予想より低いものであった。組み込み式では３～５⊿まで（特注は除く）、膜プリズムでは１～40⊿の処方が可能である。組み込み式は処方範囲が狭く度数の変更が容易ではないが、外見的に比較的目立たないこと、耐久性があることが利点である。一方膜プリズムの利点として広範囲にわたって処方が可能であり、安価で取り外しが自由にでき、症状の変化に対応しやすいことが挙げられる。しかし12⊿以上では視力低下をきたすこと[4]、高い度数では線が外見上目立つことなどが難点として報告されている[3,4]。今回処方された水平の膜プリズムの最高が左右合わせて21⊿であったことも、これらのことを裏付けていると思われる。

一旦外来でプリズムを処方しても継続して使っているとは限らない。その原因を理解することは今後のプリズム処方の適応者を知る上で重要であろう。実際、今回の調査ではプリズムを勧めた対象のうちわずか1/3、プリズムの装用トライアルを行ったうちの１/2がプリズムに満足しただけであった。

今回、プリズムに適応しやすい症例とそうでない症例を事前に知ることができれば、処方のために費やす時間と労力を軽減できるのではないかと期待して調査を行った。重度の動眼神経麻痺、重度の外転神経麻痺などの50⊿を超えるような大角度の斜視、抑制があり複視の自覚のない症例は含まれていない。また今回の調査は前向き試験でなく、カルテからの後ろ向き調査であったことから、水平、上下方向のプリズムに適応できる最大値を求めることは不可能であった。逆に、わずか１⊿であっても満足する人が存在することから、上下プリズムの重要性を認識することとなった。

満足して装用できるプリズム度数の平均値が水平方向10⊿、上下方向３⊿であること、プリズムに満足できる上下斜視角の範囲が14⊿以下であり、実際に処方された上下方向のプリズムの最高が左右合わせて５⊿であること、若年者の上斜筋麻痺ではプリズムに満足しにくいことなどが明らかになった。これらの情報は今後プリズム装用を勧める患者を選択する上で、参考になると思われる。膜プリズム、組み込みプリズムの特性を熟知したうえで、一例一例丁寧に対応することが処方の近道と考える。

参考文献

1）清水みはる，菅澤　淳，中村桂子，澤ふみ子，渡邊敏夫，池田恒彦：成人の複視に対するフレネル膜プリズムの処方．日本弱視斜視学会雑誌　29：35-38，2002.

2）高木満里子：複視に対する光学的治療　プリズム治療．日視会誌　31：67-73，2002

3）Suzanne　Veronneau-Troutman，不二門　尚，斎藤純子訳：プリズムと斜視．文光堂，東京，1998.

4）馬嶋　孝：フレネル膜プリズムとそれによるOrthoptics．眼臨　67：16-22，1973.

あたらしい眼科 23(6)：699～700，2006

もっと知りたい，斜視・弱視

More About Strabismus and Amblyopia

佐藤美保*

斜視や弱視は「なんとなくとっつきにくい」といわれる．もっとも臨床としての斜視や弱視は，診断までのプロセスはほぼ確立されているし，治療方法にしてもそれほど大きな変化はないために，一般の臨床レベルで斜視・弱視を扱うことは決してむずかしいことではない．しかし，それが「学問」，「科学」として斜視や弱視に取り組もうと考えると，とたんに「とっつきにくい」分野となる．

その理由としては，まず斜視や弱視をEBM (evidence-based medicine) で評価することが困難であることがあげられる．「視力」という自覚的に認識されやすくまた，数値化しやすい視機能と比べて，立体視や融像といった両眼視機能は自覚されることが少なく，数値化も困難である．また，両眼視は眼球のなかで結論がでないことが問題を複雑にしている．単眼視と両眼視を比べるとき，その能力は決して1+1=2という計算式では求めることができない．多くの複雑な視覚情報処理機構が脳内で行われているため，短絡的に結論を出すことができず，あれもこれもと考えているうちに，研究から離れてしまう，ということであろう．

今回の特集では上記のことを踏まえたうえで，斜視や弱視について基礎から臨床，あるいは疫学までと，一歩踏み込んだ情報を提供していく．

長谷部　聡先生には，岡山大学で行っている近視進行予防研究の中間報告を兼ねて，小児の累進眼鏡の実際について述べていただいた．眼鏡を処方する際の，チェックポイントとして，オートレフラクトメータの管理を含めた臨床的な話題である．

瀧畑能子先生は，三歳児健診を含め，小児眼科診療のレベルアップのために，全国の施設で小児眼科診療の指導にあたっておられ，実際に各地方自治体での三歳児健診に対する取り組みの違いを実感しておられる．今回は三歳児健診の現状について日本眼科医会の報告をもとに，貴重なデータを示していただいた．

脳の視覚情報処理に関する研究が進んでいる．古くはHubelとWieselによって始められた動物実験が，今ではファンクショナルMRIを用いて，ヒトの脳の視覚情報処理機構さえも明らかになってきているのである．もっとも歴史上の大発見も，視覚生理学から離れている人たちには新鮮な知識となるであろう．世界のトップレベルの研究内容を仲泊　聡先生・増田洋一郎先生にわかりやすく解説していただいた．

両眼視というと，まず立体視を思い浮かべる人が多い．立体視は中心窩の機能であるが両眼視機能には，中心窩でなく，むしろ周辺で機能するものもある．それがbinocular summationといわれるもの

* Miho Sato：浜松医科大学眼科学教室

0910-1810/06/¥100/頁/JCLS

で，この機能によってわれわれは，「もっと良く見る」ことが可能になる．Binocular summationの概念はややとっつきにくく，専門的な感があるが，両眼視機能を理解するためには，必須の知識である．この分野で多くの研究を進めている視能訓練士の若山暁美先生に解説していただいた．

過去10年間の斜視のなかで最も理解が深まった疾患の代表的なものがDuane症候群ではないだろうか．画像診断によって外転神経の走行が描出可能になったこと，遺伝学の進歩により，Duane症候群の原因遺伝子が明らかになりつつあることが大きな理由である．大庭正裕先生には，Duane症候群に伴うup-down shootに対する知見も含めて最新の知見を紹介していただいている．

高木峰夫先生・三木淳司先生には，現在も議論が多く，またそれゆえに誤解もされやすい甲状腺眼症についてEBMを踏まえて書いていただいた．文献を正しく読んで，自分のなかで判断をくだすことの大切さがが，わかっていただけると思う．

岡　真由美先生には，斜視患者のかかえる問題を評価するにあたって，眼位や眼球運動，複視だけでなく，日常生活から判断する方法を教えていただいている．このように一人の患者さんを多くの角度から評価することが，治療効果の判定や治療方法の改善につながっていくことを期待する．

野村耕治先生には，診断，治療が最も困難な斜視の代表である交代性上斜位について，臨床的な特徴から治療方法までを詳しくまとめていただいた．非常に安定した術後結果を示していただいたので，臨床の参考になると思う．

今回の特集では，さまざまな方向から斜視・弱視研究に一歩踏み込んだ内容を記載していただいている．一人でも多くの読者が斜視・弱視研究に興味を抱いていただければ幸いである．

Jpn J Ophthalmol 2006;50:323–333
© Japanese Ophthalmological Society 2006

DOI 10.1007/s10384-006-0336-y

CLINICAL INVESTIGATION

Intensity Analysis of Hartmann-Shack Images in Cataractous, Keratoconic, and Normal Eyes to Investigate Light Scattering

Toshifumi Mihashi[1,4], Yoko Hirohara[1,4], Kenichiro Bessho[1], Naoyuki Maeda[2], Tetsuro Oshika[3], and Takashi Fujikado[1]

[1]Department of Visual Science, Osaka University Graduate School of Medicine, Osaka, Japan; [2]Department of Ophthalmology, Osaka University Graduate School of Medicine, Osaka, Japan; [3]Department of Ophthalmology, University of Tsukuba, Tsukuba, Japan; [4]Technical Research Institute, Topcon Corporation, Tokyo, Japan

Abstract

Purpose: A clinical investigation of novel methods for evaluating light scattering using a Hartmann-Shack aberrometer.

Methods: Aberrometry was performed on normal eyes ($n = 7$; patient age, 26.7 ± 2.5 years, mean ± SD), eyes with keratoconus ($n = 22$; patient age, 26.1 ± 8.1 years), and eyes with cataract ($n = 17$; patient age, 56.5 ± 16.9 years) using a Hartmann-Shack wavefront aberrometer. We introduced two methods: (1) a contrast method, in which we calculated the inverse of contrast of the local images around 12 spots in a Hartmann-Shack image, and (2) a difference of point spread function (PSF) method, in which we analyzed the difference between the width of the PSF computed with aberration information and the width of the measured PSF, which contains both aberration and light scattering information.

Results: The inverse contrast in cataractous eyes (5.04 ± 3.06 inverse contrast units) was significantly larger than that in normal eyes (1.57 ± 0.56) or keratoconic eyes (1.83 ± 0.79). The difference of PSF in cataractous eyes (81.8 ± 65.2 μm) was also significantly larger than that in normal eyes (9.3 ± 4.3 μm) or keratoconic eyes (30.0 ± 20.1 μm). The inverse contrast and the difference in the PSF were highly correlated ($r = 0.89$, $P < 0.0001$).

Conclusions: The two methods introduced here successfully distinguished cataractous eyes from normal and keratoconic eyes. After the results were analyzed by a discriminant analysis, the separation of the three categories proved to be excellent. **Jpn J Ophthalmol** 2006;50:323–333 © Japanese Ophthalmological Society 2006

Key Words: cataract, light scattering, Hartmann-Shack wavefront aberrometer, point spread function, wavefront aberration.

Introduction

Vision is affected not only by geometrical optical aberrations and diffraction but also by light scattering. Vision in elderly or cataract patients is considered to be more affected by light scattering by the crystalline lens than that in young people.[1,2] We developed two methods for analyzing Hartmann-Shack images to investigate not only higher order aberrations but also light scattering by the crystalline lens.

A Hartmann-Shack wavefront aberrometer is used to measure higher order aberrations in the human eye.[3,4] Wavefront sensing is useful technology for customized corneal refractive surgery[5] and adaptive optics.[6,7] It is also valuable clinically for diagnostic purposes in patients with keratoconus,[8] cataract,[9,10] or dry eye.[11,12] If wavefront aberration and light scattering could be measured simultane-

Received: September 6, 2005 / Accepted: January 23, 2006
Correspondence and reprint requests to: Takashi Fujikado, Department of Visual Science, Osaka University Graduate School of Medicine, Room G4, 2-2 Yamadaoka, Suita, Osaka 565-0871, Japan
e-mail: fujikado@ophthal.med.osaka-u.ac.jp

Jpn J Ophthalmol
Vol 50: 323–333, 2006

ously, evaluation of the optical quality of the eye would be more efficient and convenient than is the case when separate evaluation methods are used clinically.

Various methods have been proposed and used for evaluating light scattering of the eyes. Although a contrast sensitivity test is a good subjective measurement method for detecting a subtle degradation of vision,[1] other objective methods such as a slit-lamp examination are required to determine whether the image degradation is due to light scattering by the lens.[13,14] A specific psychometric method, which uses a flickering light source in the peripheral region of the subject's visual field, has also been developed and used to successfully measure the effect of aging on light scattering.[15]

Intensity analysis of Hartmann-Shack images measured by a Hartmann-Shack wavefront aberrometer can be used as an objective method of estimating light scattering by the lens.[16–19] We used two methods of analysis in this study. The first method involves measuring the contrast of the image obtained with the Hartmann-Shack wavefront aberrometer. The second method involves measuring the width of the point spread function (PSF), that is, the local intensity around each spot, and calculating the difference between the measured widths of the PSFs and the widths of PSFs computed from the aberrations.

We applied these methods to normal eyes, which are eyes with small aberrations and little light scattering; keratoconic eyes, which are eyes with large aberrations but little light scattering; and cataractous eyes, which are eyes with small aberrations but much light scattering. The results of this analysis were evaluated using statistical methods, including a discriminant analysis.[20] The results were also evaluated by comparing the angular characteristics of typical Mie scattering, diffraction, and wavefront aberration. Our final goal in developing these methods was to provide simple and easy ways to quantitatively evaluate cataractous eyes.

Subjects and Methods

Subjects

Subjects in the study were consecutive patients who had solid wavefront measurements performed during examinations at Osaka University Hospital between October 2000 and August 2001. Their eyes were measured three times at the visit, and all three of those measurements were analyzed. Twenty-five eyes of 15 patients (age, 26.1 ± 8.1 years, mean ± SD; range, 14–50 years) were keratoconic. The best-corrected visual acuity (BCVA) ranged from 20/100 to 20/13. Seventeen eyes of nine patients (age, 56.5 ± 16.9 years; range, 24–70 years) were cataractous. Fourteen eyes were classified as mild cortical-dominant cataractous [nuclear opalescence (NO), 1.0–2.0, mean, 1.3 ± 0.4; nuclear color (NC), 1.0–2.0, mean, 1.8 ± 0.4; cortical cataract (C), 2.0–3.0, mean, 2.2 ± 0.4; Lens Opacities Classification System III scale]. Three eyes were mild nuclear-dominant cataractous (NO, 3.0–4.0; NC, 2.0–3.0; C, 1.0–2.0). The BCVA ranged from 20/200 to 20/20. Eight eyes of eight normal subjects (age, 26.7 ± 2.5 years; range, 21–32 years) were also included in the study.

Excluded from the study were eyes for which Hartmann-Shack images could not be analyzed automatically by the aberrometer, eyes with superficial keratopathy, and eyes with a corneal scar.

Written informed consent was obtained from all participants in accordance with the tenets of the Declaration of Helsinki.

Measurement of Aberrations Using the Hartmann-Shack Wavefront Aberrometer

A Hartmann-Shack wavefront aberrometer, a prototype of KR9000PW (Topcon, Tokyo, Japan) was used.[10] A simplified schematic diagram of the optics for measuring wavefront aberrations is shown in Fig. 1. The Hartmann-Shack wavefront sensor consists of a Hartmann-Shack lenslet array and a charge-coupled device (CCD). Because the output of the CCD is linearly calibrated with the intensity of the input light over its measurement range, the light intensity of the Hartmann-Shack image is known immediately after measurement. The lenslet array consists of 163 lenslets, each of which is an eight-level binary optical element (BOE: lenslet size, 0.6 mm × 0.6 mm; focal length, 40 mm; diffraction efficiency, 90%[21]) especially designed for the aberrometer and fabricated in the Topcon factory. The light source is a high-luminance diode device with a central wavelength of 840 nm (=0.84 μm) and a half-width at half maximum of 20 nm. The module is attached to a polarized mode-preserved single-mode optical fiber, and the diameter of the core is 5.5 μm. We assumed the end of the fiber to be a point light source for wavefront sensing. When the unit was used to measure the refraction and aberrations, the fundus was adjusted to be conjugate with the end of the fiber by moving the internal optics. A rotating wedge-shaped prism was set in the common path of ingoing and outgoing light to scan the light beam on the fundus. The wavelength band of the light source and the rotating wedge-shaped prism reduced unwanted speckle and averaged the orientation and spatial discrepancy of reflectance from the fundus. As the scan was made by rotation of the wedge-shaped prism, the path of the image of the point light source was seen as a ring on the fundus. The diameter of the ring was 32 min of visual angle on the fundus, because with this small angle the optics do not induce any significant aberrations that would produce artifacts in the measurements. As the image of the light source was being scanned on the fundus, image I1 (Fig. 1) and images I2, which were on the CCD of the Hartmann-Shack wavefront sensor, were not moving but formed stable point images, because the rotating wedge-shaped prism was set in the common path of the ingoing and outgoing rays. As shown in Fig. 1, when the ingoing rays refracted slightly downward at the rotating wedge-shaped prism, the outgoing rays reflected from the fundus returned to the original angle at the wedge-shaped prism. The outgoing rays always

returned to the original angle when the ingoing rays were refracted upward or in any other direction at the wedge-shaped prism. Although this is guaranteed exactly only at the Gaussian optics (1st order) level, we designed and manufactured virtually aberration-free optics to maintain this characteristic for real ingoing and outgoing rays. This was confirmed experimentally with model eyes with refraction ranges from −15 to +15 D, and it was also confirmed by the images we obtained, including the images shown in Fig. 2. In our experience, ring-shaped images are never observed in Hartmann-Shack images.

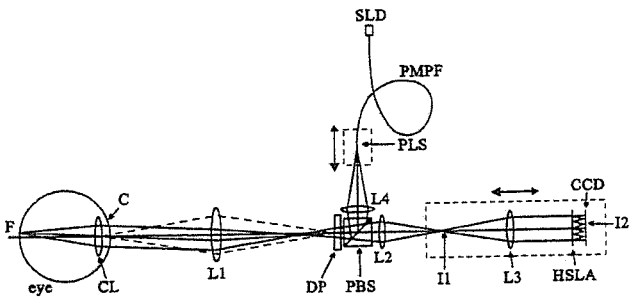

Figure 1. Schema of the Hartmann-Shack wavefront aberrometer, a prototype of KR9000PW (Topcon, Tokyo, Japan). *HSLA*, Hartmann-Shack lenslet array; *PBS*, polarized beam splitter; *SLD*, superluminescent diode; *PLS*, point light source; *PMPF*, polarized mode-preserved single-mode optical fiber; *DP*, rotating wedge-shaped prism; *C*, cornea; *CL*, crystalline lens; *F*, fundus; *CCD*, charge-coupled device. L1, L2, L3, and L4 are lenses or a group of lenses. I1 and I2 are images or a group of images. The fixation target and its optics, and the optics used to observe the anterior segment of the eye are omitted from the schema for simplification.

Because the rotating wedge-shaped prism was optically conjugate with the entrance pupil of the eye, the front focus of lens L1 and L2 combined (Fig. 1) was on the entrance pupil of the eye, and the back focus of lens L3 was on the Hartmann-Shack lenslet array. The conjugate relation between the entrance pupil of the eye and the Hartmann-Shack lenslet array was always maintained while the wedge-shaped prism was rotating and lens L3 and the Hartmann-Shack wavefront sensor were moving to adjust the refraction of the eye. Thus, the local information on wavefront aberration from the Hartmann-Shack wavefront sensor always reflected the corresponding local wavefront information on the pupil of the eye.

To determine the wavefront aberrations with the Hartmann-Shack wavefront aberrometer, the positions of the spots in the Hartmann-Shack image were used to calculate the slopes of rays from the lenslet array. The relation between the slopes and the wavefront is expressed by the following equations:

$$\frac{\partial W(X,Y)}{\partial X} = \frac{\Delta x}{f}, \qquad \frac{\partial W(X,Y)}{\partial Y} = \frac{\Delta y}{f}, \tag{1}$$

where $W(X, Y)$ is the wavefront, X and Y are the horizontal and vertical coordinates on the pupil, respectively, Δx and Δy are the displacements of the spots from their reference positions on the CCD, and f is the distance between the Hartmann-Shack lenslet array and the CCD. We used Zernike expansions up to the fourth order to represent wavefront aberration.

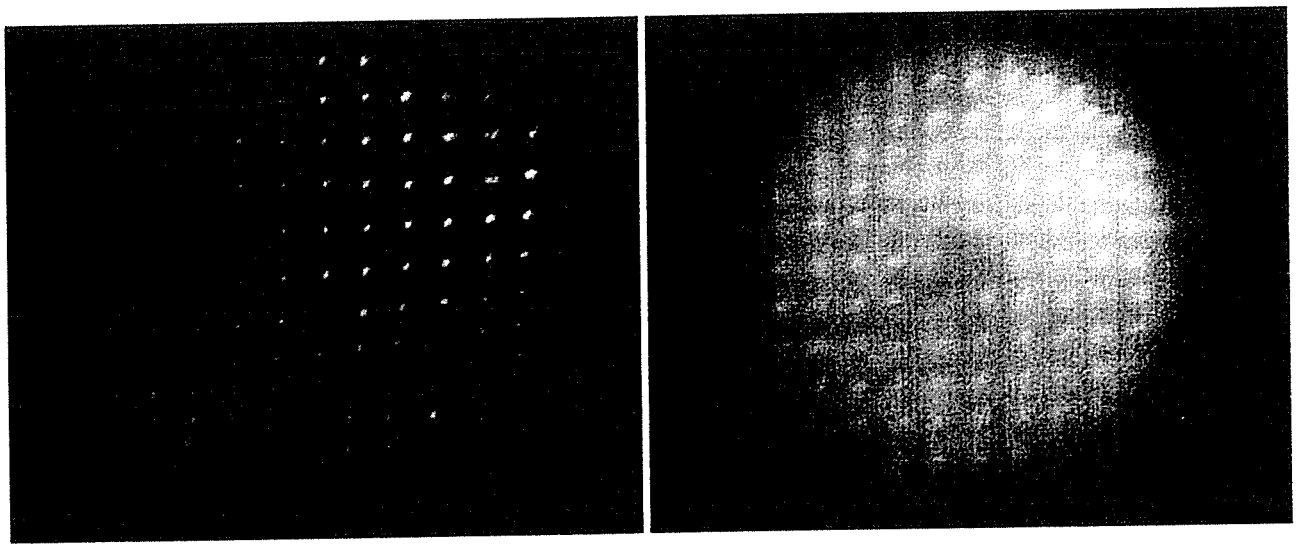

(a) keratoconus (b) cataract

Figure 2a, b. Hartmann-Shack images of (**a**) a keratoconic eye and (**b**) a cataractous eye. The root mean square (RMS) of the wavefront aberrations for the central 4-mm pupillary area was 0.757 μm in the keratoconic eye and 0.277 μm in the cataractous eye. Even though the aberrations of the cataractous eye were smaller than those of the keratoconic eye, the image of the cataractous eye is more blurred than that of the keratoconic eye.

Jpn J Ophthalmol
Vol 50: 323–333, 2006

$$W(x,y)=\sum_{n=1}^{4}\sum_{m=-n,-n+2,}^{n} c_n^m \cdot Z_n^m(x,y) \quad (2)$$

where c_n^m is the coefficient of each Zernike polynomial $Z_n^m(x,y)$, and n and m represent the radial order and azimuth order, respectively. We substituted into equation (2) $W(x,y)$ of equation (1) to find c_n^m using the least-squares method.

When, for example, we refer to a "fourth-order wavefront aberration," we mean the sum of the terms with $n = 4$ in equation (2). The root mean square (RMS) value of the wavefront aberration is the square root of the sum of all included terms when we use normalized Zernike polynomials. In this article, we call this measurement the "classical wavefront measurement" following Thibos and Hong.[16]

Contrast Method

Hartmann-Shack images of cataract and keratoconic eyes obtained by the Hartmann-Shack wavefront aberrometer are shown in Fig. 2. The background intensity of the cataract image was brighter than that of the keratoconus image. It is reasonable that an increase of Rayleigh-Gans scattering or Mie scattering is related to an increase of the background intensity of the Hartmann-Shack image, causing the decrease in image contrast.

The contrast around each spot was analyzed from the images obtained by the CCD of the Hartmann-Shack wavefront sensor. Figure 3 shows the schema for this evaluation (a single sample area is the square area surrounded by the dashed lines). Twelve spots around the center of the pupil (corresponding to the area of a 4-mm pupil) were measured, and the local maximum intensity and local minimum intensity were found for each 0.6 mm × 0.6 mm square area. The Michelson contrast over the 12 spots was defined as follows:

$$Contrast=\frac{1}{N}\sum_{i=1}^{N}\frac{Imax_i-Imin_i}{Imax_i+Imin_i} \quad (3)$$

where $Imax_i$ indicates the maximum image intensity, and $Imin_i$ indicates the minimum image intensity (background intensity) in the area of i-th point, and N is the number of spots. Finally, we used the inverse of the contrast to represent degradation of optical quality.

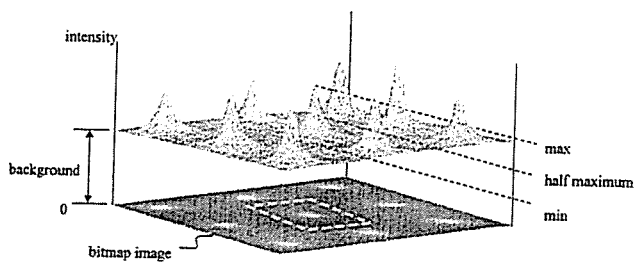

Figure 3. Light intensity around the spots of the Hartmann-Shack image. Minimum and maximum intensities around a spot corresponding to that on the Hartmann-Shack image are schematically shown. The half maximum was defined after the background intensity was subtracted from the image intensity.

Although in Fig. 2a there seems to be more blur in the peripheral region of the pupil, and this region would have additional information on contrast, only the central 4-mm region was used in the contrast method (and in the following PSF method) because many cataractous eyes are aged eyes with small pupils. Hence, we limited pupil size to an area 4 mm in diameter in this study.

The results from an artificial eye were used for calibration. The scattering from the lens of the artificial eye was negligible; thus, any measured scattering with the artificial eye could be assigned to the optics of the aberrometer. The light scattering was quantified by computing the inverse of the contrast in equation (3).

PSF Method

The spots in the cataract image were more blurred than those in the keratoconus image (Fig. 2), although aberrations from the second to fourth order of the cataractous case were smaller than those of the keratoconus case. Thus, this blur was too large to be explained by the wavefront aberration that we measured using the Hartmann-Shack wavefront aberrometer.

Although the cause of the larger blur was not clear, to distinguish this blur from the expected amount of blur caused by wavefront aberrations of up to the fourth order and diffraction, widths of two kinds of PSFs were compared, although this comparison is not theoretically rigorous but rather one of convenience. One PSF was obtained by measuring the intensity distribution of the area around the corresponding spot in the Hartmann-Shack image. This PSF was referred to as the "measured PSF." The other PSF was obtained by a three-step numerical calculation from the measured wavefront aberration; namely, the PSF formed on the fundus by the ingoing path (step 1) and the PSF formed on the CCD by the outgoing path (step 2) were calculated, and then the total PSF was found by combining the two calculations of the ingoing PSF and outgoing PSF (step 3). We refer to this PSF as the "computed PSF."

As illustrated in Fig. 4, the light beam forming the PSF on the fundus was affected by diffraction, aberration, and forward light scattering of the ocular optics. We assumed that the "forward light scattering" had a broad meaning, including scattering by very large particles. We also included very high order wavefront aberration as a cause of forward light scattering, for convenience in this study. Refractive-index fluctuations of the very large particles and very high order wavefront aberrations are not exactly the same, but they can share the same spatial frequency range, which induces narrow-angle forward light scattering. Pierscionek et al.[22] showed that aberrations and scattering can be simulated by using phase plates. A light beam reflected from the fundus forming the PSF on the CCD is again affected by diffraction, aberration, forward scattering of the ocular

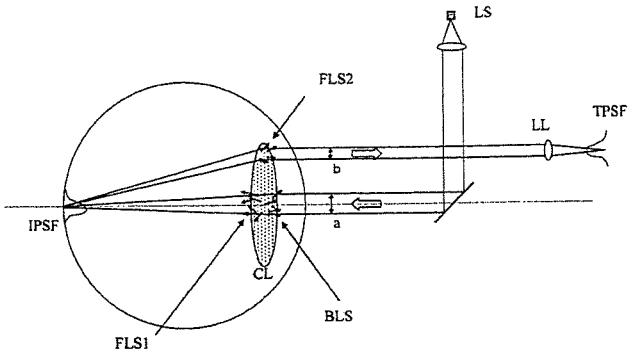

Figure 4. A schematic figure to explain the factors that influence image formation in the eye. Causes of the light scattering were categorized into forward light scattering from the ingoing beam area to the retina (*FLS1*), backward light scattering from the ingoing beam area toward the Hartmann-Shack wavefront sensor (*BLS*), and forward light scattering from the outgoing beam area toward the Hartmann-Shack wavefront sensor (*FLS2*). *LS*, light source; *CL*, crystalline lens; *IPSF*, ingoing point spread function; *LL*, lenslet array of the Hartmann-Shack wavefront sensor; *LS*, light source; *TPSF*, total point spread function; *a*, the circular entrance aperture (diameter, 1.1 mm); *b*, one of the square exit apertures (0.6 mm × 0.6 mm).

optics by the outgoing light, and back scattering of the ocular optics by the ingoing light.

The computed PSF is affected only by diffraction and aberration, but not by light scattering. The difference between the two PSFs thus represents the influence of light scattering from both ingoing and outgoing light.

The PSF width (=square root of the area) was used to compare the two PSFs. The area of the measured PSF was the area in which light intensity was larger than the half-maximum of the PSF. The background intensity, which is schematically shown in Fig. 3, was eliminated before the analysis.

PSFs were calculated from measured wavefront aberrations using scalar diffraction theory.[23] We used a fast Fourier transform to calculate PSFs, assuming a small aberration, because the sizes of the apertures were 1.1 mm (diameter) for the ingoing light and 0.6 mm (one side of a square) for the outgoing light (see Fig. 4). The diameter of the aperture for the ingoing optical path was 1.1 mm, and was determined by an internal stop in the aberrometer. Because the equivalent focal length of the eye in air is 17 mm, the ingoing PSF is,

$$PSF_{IN}(x,y) = \left| \int_{-\sqrt{0.55^2-x^2}}^{\sqrt{0.55^2-x^2}} \int_{-0.55}^{0.55} \exp\left(-\frac{2\pi i}{\lambda} \sum_{i=1}^{4} \sum_{j=-i,-i+2,}^{i} C_i^j Z_i^j\left(\frac{1}{2}X, \frac{1}{2}Y\right) \right) \cdot \exp\left(-\frac{2\pi i}{\lambda \cdot 17}(xX + yY) \right) dXdY \right|^2 \quad (4)$$

where X and Y are pupil coordinates. In a classical wavefront measurement, the coefficients C_i^j of the Zernike polynomials $Z_i^j(x,y)$ up to the fourth order of the wavefront aberrations were measured for a 4-mm-diameter pupil. In this equation, the wavefront aberration for the 4-mm pupil is reconstructed, and a portion of the wavefront is used for the PSF calculation. The wavelength for wavefront sensing, λ, was 840 nm (0.00084 mm). The definite integral of equation (4) was numerically calculated over the circular area corresponding to the entrance beam.

Apertures of the outgoing path were 0.6 mm × 0.6 mm; the distance between the pupil and the CCD was 40 mm. We again used Zernike polynomials $Z_n^m(x,y)$ up to the fourth order for a 4-mm pupil to calculate the outgoing PSF,

$$PSF_{OUT\,i}(x,y) = \left| \int_{-0.3}^{0.3} \int_{-0.3}^{0.3} \exp\left(-\frac{2\pi i}{\lambda} \sum_{l=1}^{4} \sum_{m=-l,-l+2,}^{l} C_l^m Z_l^m\left(\frac{1}{2}(X-a_i), \frac{1}{2}(Y-b_i)\right) \right) \cdot \exp\left(-\frac{2\pi i}{\lambda \cdot 40}(xX + yY) \right) dXdY \right|^2 \quad (5)$$

where a_i and b_i are locations of the lenslets, and i is a subscript indicating the i-th lenslet on the Hartmann-Shack lenslet array. The definite integral was numerically calculated over the rectangular area corresponding to each lenslet.

We assumed that the phase of the ingoing light was not maintained in the outgoing light after the light beam was reflected from the fundus. The PSF obtained by the Hartmann-Shack wavefront sensor is a convolution of the ingoing PSF and outgoing PSF,

$$PSF_{total\,i}(x,y) = \iint PSF_{IN}\left((x-u)/\beta, (y-v)/\beta\right) \cdot PSF_{OUT\,i}(u,v)\,dudv \quad (6)$$

where $PSF_{total\,i}$ is the PSF of the total optics corresponding to the i-th lenslet, PSF_{IN} is ingoing PSF and $PSF_{OUT\,i}$ is the related outgoing PSF.[24,25] β is the PSF magnification of the optics between the fundus and the CCD, which was −2.30 in this case. Although the internal optics of the Hartmann-Shack wavefront aberrometer were adjusted to achieve the best focus for refraction of each eye and the amount of adjustment varied with the PSF magnification, the variation was less than 4% of the magnitude.

We assumed that the equivalent focal length was 17 mm. This value depends on the individual eye. However, in this analysis, the PSF magnification was inversely proportional to the focal length, so the absolute value of the focal length was eliminated from the results. We used this value in equations 4 and 5 for explanatory purposes.

We subtracted the width of the computed PSF from the width of the measured PSF to discern the effect of light scattering from diffraction and the aberrations. We used the average of 12 PSFs (corresponding to the area of a 4-mm pupil; $N = 12$ in the equation),

$$\text{difference of PSF} = \frac{1}{N}\sum_{i}^{N}\left\{\left(\text{width of PSF}_{\text{measured}}\right)_i - \left(\text{width of PSF}_{\text{computed}}\right)_i\right\} \quad (7)$$

Simulation of Light Scattering

To determine the angular characteristics of Mie scattering by spherical particles, a rigorous solution exists. The theory and a program to compute it are well documented in a textbook,[26] and ready-to-use programs are even available on the Internet.[27] Here, we comment briefly on the theory of Mie scattering. Because Mie scattering concerns scattering by a spherical particle, the coordinate system chosen is spherical polar coordinates. We can find a solution of the wave equation of an electromagnetic field in spherical polar coordinates by using the method of separation of variables. After finding the form of the solution equation, we need to find a solution that satisfies the boundary conditions at the surface of the spherical particle. We need an efficient numerical method to calculate the final solution with a personal computer.

Such a method has been developed.[26] The size of the particle and refractive indices outside and inside the particle are important parameters in the analysis. The sizes of the particles used were 0.7 μm and 4 μm. These are typical sizes of particles that induce Mie scattering in a crystalline lens.[28,29] In this study, we were interested in the scattering of the measurement light of the Hartmann-Shack wavefront sensor. We used a wavelength of 840 nm and unpolarized light for the calculation. The ratio of the refractive indices between the particle and its surroundings was 1.1.[29,30]

Angular characteristics from diffraction and aberration were evaluated with equation 4. The PSF on the fundus was simulated using this equation. In this simulation, Zernike coefficients of one of the keratoconic eyes in the study with the largest aberrations were used.

Data Analysis

All statistical tests were carried out with the software package Statview Version 5.01 (SAS Institute, Cary, NC, USA) or SPSS Version 12 (SPSS, Chicago, IL, USA). We used 95% confidence limits.

Results

Wavefront Aberrations

The RMS value of third- and fourth-order wavefront aberrations in a 4-mm pupil area was 0.078 ± 0.044 μm (mean ± SD) for the normal eyes, 0.347 ± 0.239 μm for the keratoconic eyes, and 0.230 ± 0.098 μm for the cataractous eyes. A statistically significant difference was found among those three groups [analysis of variance (ANOVA), $DF = 2$, $F = 7.119$, $P = 0.0021$). However, a statistically significant difference was found only between normal and keratoconic eyes in the post hoc test (Scheffé test, *Mean Diff* = 0.268 μm, $P = 0.0027$).

Contrast Method

Figure 5 shows the results of the image contrast measurements. In each graph, the horizontal axis represents the magnitude of third- and fourth-order wavefront aberrations, and the vertical axis is the inverse of the image contrast. As the inverse of the image contrast was used to represent the light scattering quantitatively, a larger value represents a larger degree of light scattering.

The inverse of contrast in the 4-mm pupil area was 1.57 ± 0.56 (mean ± SD) for the normal eyes, 1.83 ± 0.79 for the keratoconic eyes, and 5.04 ± 3.06 for the cataractous eyes. Among them, a significant statistical difference was found (ANOVA, $DF = 2$, $F = 15.554$, $P < 0.0001$).

The inverse contrast of cataractous eyes was significantly larger than those of normal eyes (Scheffé test, *Mean Diff* = 3.467, $P = 0.0007$) and of keratoconic eyes (Scheffé test, *Mean Diff* = 3.205, $P < 0.0001$), while the inverse contrast of normal eyes and that of keratoconus eyes were not significantly different (Scheffé test, *Mean Diff* = 0.262, $P = 0.9479$).

There was no significant correlation between inverse contrast and third- and fourth-order wavefront aberrations for keratoconic eyes ($r = 0.087$, $P = 0.700$) or cataractous eyes ($r = 0.142$, $P = 0.587$).

We linearly transformed the two axes in Fig. 5a or b to the canonical discriminant functions in Fig. 5c for better separation. Using the squared Mahalanobis distance between each sample point and the group centroid, the analysis classified 84.0% of the originally grouped cases correctly. We used separate group covariance matrices for the canonical discriminant functions. Results are shown in Table 1.

PSF Method

Figure 6 shows the relation between the scattering that was calculated with equation 6 and the third- and fourth-

Table 1. Classification results after discriminant analysis with SPSS of contrast method data

Eye type	Normal region	Keratoconic region	Cataractous region
Normal	8 (100%)	0 (0%)	0 (0%)
Keratoconic	3 (12%)	19 (76%)	3 (12%)
Cataractous	1 (6%)	1 (6%)	15 (88%)

84.0% of originally grouped cases were correctly classified.

(a)

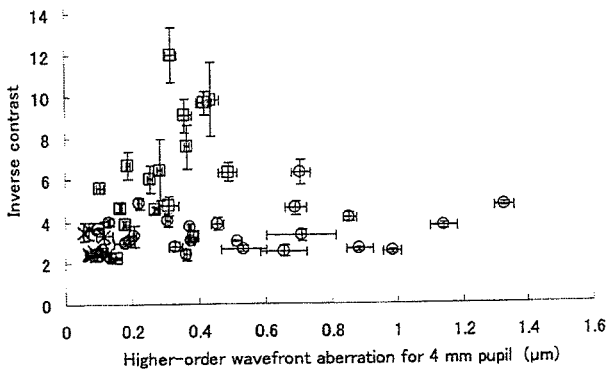

(b)

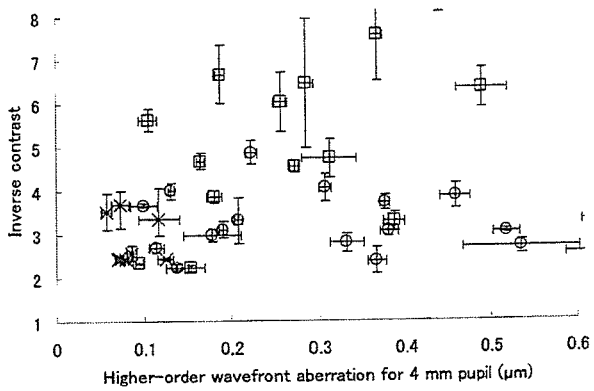

(c)

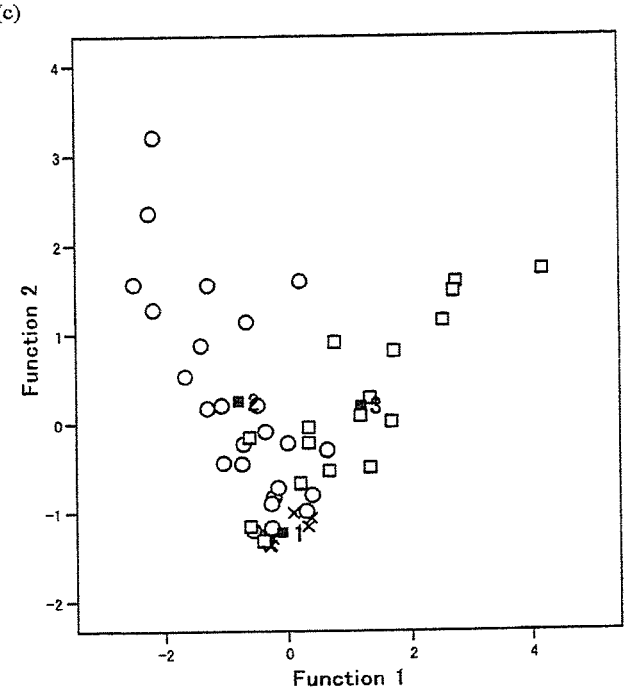

Table 2. Classification results after discriminant analysis with SPSS of difference of PSF data

Eye type	Normal region	Keratoconic region	Cataractous region
Normal	8 (100%)	0 (0%)	0 (0%)
Keratoconic	2 (8%)	17 (68%)	6 (24%)
Cataractous	1 (6%)	2 (12%)	14 (82%)

78.0% of originally grouped cases were correctly classified
PSF, point spread function

order wavefront aberrations. All data values except one (=–0.96 μm) were positive.

The difference in PSFs in the 4-mm pupil area was 9.3 ± 4.3 μm (mean ± SD) for the normal eyes, 30.0 ± 20.1 μm for the keratoconic eyes, and 81.8 ± 65.2 μm for the cataractous eyes. A statistical difference was found among them (ANOVA, $DF = 2$, $F = 10.983$, $P = 0.0001$).

The difference in the PSFs of cataract eyes was significantly larger than that of normal eyes (Scheffé test, *Mean Diff* = 73, $P = 0.0009$) or keratoconic eyes (Scheffé test, *Mean Diff* = 52, $P = 0.0017$), while those of normal eyes and keratoconus eyes were not significantly different (Scheffé test, *Mean Diff* = 21, $P = 0.4911$).

There was no significant correlation between the differences of PSF and the third- and fourth-order wavefront aberrations: $r = 0.328$ ($P = 0.136$) for keratoconic eyes and $r = 0.309$ ($P = 0.227$) for cataractous eyes.

Again, we linearly transformed the two axes of Fig. 6a or b to the canonical discriminant functions in Fig. 6c for better separation. Using the squared Mahalanobis distance between each sample point and the group centroid, the analysis classified 78.0% of the originally grouped cases correctly. Results are shown in Table 2.

Simulation of Light Scattering

Results of Mie scattering simulations are shown in Fig. 7. The half-width at half height of the scattering function by a 0.7-μm particle is 18.8° and that for a 4-μm particle is 2.8°.

Simulations of diffraction and wavefront aberration are shown in Fig. 8. The half-width at half height of the PSF for a keratoconic eye was 0.02°, which was much narrower than that of the scattering from the particles.

Figure 5a–c. Light scattering evaluated by the contrast method. The horizontal axis is the RMS of third- and fourth-order wavefront aberrations for the central 4-mm pupillary area. The vertical axis is the inverse contrast. Normal eyes (×), keratoconic eyes (○), and cataractous eyes (□) are shown. Error bars designate standard errors. **a** and **b** are the same graph but **b** is expanded to show small values clearly. **c** Graph with canonical functions generated by an SPSS discrimination analysis. Data were divided into three groups so that each data point has the smallest Mahalanobis distance between its position and the corresponding group centroid. ■1 is the centroid of the normal group, ■2 is that of the keratoconic group, and ■3 is that of the cataractous group.